Published in final edited form as:
Analyst. 2013 October 7; 138(19): 5654–5664. doi:10.1039/c3an01113e.

Optimization of microfluidic PET tracer synthesis with Cerenkov imaging†

Alex A. Dooraghi[a,b,‡], **Pei Y. Keng**[a,b,‡], **Supin Chen**[c], **Muhammad R. Javed**[a,b], **Chang-Jin "CJ" Kim**[d], **Arion F. Chatziioannou**[a,b], and **R. Michael van Dam**[a,b]

[a]Crump Institute for Molecular Imaging, University of California, Los Angeles (UCLA), Los Angeles, CA, U.S.A.

[b]Department of Molecular & Medical Pharmacology, University of California, Los Angeles (UCLA), Los Angeles, CA, U.S.A.

[c]Department of Bioengineering, University of California, Los Angeles (UCLA), Los Angeles, CA, U.S.A.

[d]Department of Mechanical and Aerospace Engineering, University of California, Los Angeles (UCLA), Los Angeles, CA, U.S.A.

Abstract

Microfluidic technologies provide an attractive platform for the synthesis of radiolabeled compounds. Visualization of radioisotopes on chip is critical for synthesis optimization and technological development. With Cerenkov imaging, beta particle emitting isotopes can be localized with a sensitive CCD camera. In order for Cerenkov imaging to also serve as a quantitative tool, it is necessary to understand how material properties relevant to Cerenkov emission, namely, index of refraction and beta particle stopping power, affect Cerenkov light output. In this report, we investigate the fundamental physical characteristics of Cerenkov photon yield at different stages of [^{18}F]FDG synthesis on the electrowetting on dielectric (EWOD) microfluidic platform. We also demonstrate how Cerenkov imaging has enabled synthesis optimization. Geant4, a Monte Carlo program applied extensively in high energy physics, is used to simulate Cerenkov photon yield from ^{18}F beta particles traversing materials of interest during [^{18}F]FDG synthesis on chip. Our simulations show that the majority (approximately two-thirds) of the ^{18}F beta particle energy available to produce Cerenkov photons is deposited on the glass plates of the EWOD chip. This result suggests the possibility of using a single calibration factor to convert Cerenkov signal to radioactivity, independent of droplet composition. We validate our simulations with a controlled measurement examining varying ratios of [^{18}O]H_2O, dimethyl sulfoxide (DMSO), and acetonitrile (MeCN), and find a consistent calibration independent of solvent composition. However, the calibration factor may underestimate the radioactivity in actual synthesis due to discoloration of the droplet during certain steps of probe synthesis. In addition to

†Electronic Supplementary Information (ESI) available: [details of any supplementary information available should be included here]. See DOI: 10.1039/b000000x/

Fax: 310-206-8975; Tel: 310-206-6507; MVanDam@mednet.ucla.edu.

‡Authors contributed equally to this work

the attractive quantitative potential of Cerenkov imaging, this imaging strategy provides indispensable qualitative data to guide synthesis optimization. We are able to use this imaging technique to optimize the mixing protocol as well as identify and correct for loss of radioactivity due to the migration of radioactive vapor outside of the EWOD heater, enabling an overall increase in the crude radiochemical yield from 50±3% (n=3) to 72±13% (n=5).

Introduction

Radiolabeling of compounds of interest is an attractive approach used in assays of cellular molecules,[1, 2] nuclear imaging,[3] and radiotherapeutics.[4, 5] Microfluidic devices provide ideal platforms for these applications because the devices can, in general, be easily automated and because their compact size greatly reduces the amount of radiation shielding needed to protect personnel. Several groups have demonstrated the use of microfluidic chips to perform complex multi-step chemical synthesis processes needed to produce several example PET tracers.[6–10] To mature such technologies into practical tools for routine automation of radiochemistry or biological assays requires optimization of devices and processes. This optimization requires good analytical tools capable of spatially-resolved radiation measurements at multiple time points during on-chip processes while minimizing radiation exposure to the operator.

Few tools for quantitative visualization of beta particle emitting radioisotopes in microfluidics have been investigated. A PhosphorImager system was used to image ^{68}Ga labeled peptides adsorbed on the microfluidic channels of a plastic compact disc.[11] A position sensitive avalanche photodiode (PSAPD) was presented to assay the uptake of beta particle emitting molecular probes in small populations of cells incubated in a polydimethylsiloxane (PDMS) chip.[12–14] The distribution of [^{18}F]fluoride adsorbed on a brass-platinum electrochemical micro-flow cell was visualized using autoradiography.[15] However, these techniques require the microfluidic platform to be in direct contact with the detector and to be “thin” (compared to the beta particle range) to image the radioactivity with good resolution and sensitivity. For devices made of thick materials, it may be necessary to disassemble the microfluidic device and image the internal surfaces directly, as was the case in Sadeghi *et al.*[15] Furthermore the minute volume of liquid used in a single experiment on a microfluidic chip prohibits one to obtain several kinetic samples at different time points from one batch of synthesis. Conventionally, to obtain samples for analyses at different time points, multiple sets of experiments have to be performed to achieve the desirable outcome or to optimize a particular process. To overcome these limitations, we previously reported a technique for imaging the Cerenkov radiation emitted during ^{18}F positron decay that enabled visualization and quantification of the distribution of radioactivity within PDMS microfluidic chips using a lens coupled CCD camera placed several centimeters from the chip.[16] We then used this technique[17] to understand and circumvent the variable performance in chemistry steps in these chips that have been observed by our group and others.[18, 19]

Cerenkov radiation describes photons predominantly in the UV and optical spectrum produced when a beta particle travels faster than the speed that light travels in the

surrounding medium. Cerenkov imaging has generated appeal in other areas of research. For example, Cerenkov imaging has motivated the development of a low cost, low resolution alternative to PET termed Cerenkov Luminescence Imaging.[20–27] In our proposed application for on-chip radiolabeling optimization, Cerenkov imaging can be used for chips of any thickness provided two conditions are met. First, the chip is made from transparent material. Second, the speed of light of the material is lower than the speed of the beta particles emitted by the radioisotope used for radiolabeling. Cerenkov imaging does not require additional modifications for beta particle detection as the chip material and the solvents within it are the media in which the Cerenkov photons are produced. Thus, a distinct advantage of Cerenkov imaging is the ability to monitor the chip at multiple consecutive time points *in situ*, enabling an arbitrary number of quantitative measurements during a single experiment. Cerenkov imaging is a promising tool to study the overall synthesis on the chip, to compare the loss that occurs at different stages of a process, and to monitor the rate of accumulation or release of radioisotope from surfaces.[17]

Using the synthesis of the PET tracer 2-[^{18}F]fluoro-2-deoxy-D-glucose ([^{18}F]FDG) on a digital microfluidic device as an example application,[28] we present in this paper an improved Cerenkov imaging system, a study of differences in Cerenkov light yield based on the particular liquid composition inside the chip, and describe how Cerenkov imaging enabled substantial improvement in the synthesis yield. Improvements in the imaging system were designed to increase signal to noise ratio (which can be used to increase temporal resolution), increase the range of radioactivity that can be monitored, and enable rapid switching between Cerenkov imaging and real-time video monitoring of the same device. The accuracy of quantitative Cerenkov measurements was increased by studying the fundamental physical characteristics of Cerenkov photon yield at different stages of the synthesis process. This enabled a more detailed understanding of the calibration of Cerenkov signal to radioactivity and its dependence on optical properties of the liquid and device materials. Despite the high apparent efficiency of the radiofluorination and hydrolysis reactions in our previous work, the overall radiochemical yield (ratio of amount of [^{18}F]FDG obtained from the chip relative to the starting amount of [^{18}F]fluoride ion) was low. This discrepancy suggested that there were significant losses of radioactivity during the synthesis that could be due to the formation of volatile/aerosol containing ^{18}F-labeled species. Using Cerenkov imaging, these losses were identified and corrected, resulting in an improved [^{18}F]FDG micro-synthesis process.

Experimental

2.1 Simulation

Material properties affect Cerenkov photon yield. Therefore, it is critical to understand Cerenkov photon yield for materials in a geometry relevant to EWOD in order to quantify Cerenkov emission reliably during probe synthesis. To that end, two Geant4 simulations[29, 30] were performed to determine the average number of photons per ^{18}F decay produced in the materials positrons may encounter in a typical EWOD experiment. Geant4 is capable of direct simulation of Cerenkov emission based on specifying the chemical composition, density and index of refraction of the material through which the beta particles

pass. Table 1 shows index of refraction (n_D) and density values for [^{18}O]H_2O, acetonitrile (MeCN), dimethyl sulfoxide (DMSO) and soda-lime glass. The index of refraction data as a function of wavelength for H_2O, MeCN and DMSO were determined using parameters reported in literature.[31] The glass index of refraction value was estimated to be constant using the n_D value of 1.52. The Geant4 standard physics model was used for all beta and gamma interactions, enabling secondary particle generation. The Cerenkov emission acceptance wavelength range was 400–1000 nm.

Simulation 1 (S1) was performed in order to understand Cerenkov emission yield from bulk amounts of material of interest to serve as a comparison with simulation 2 (S2), which takes into consideration the EWOD geometry. For S1 (Fig. 1a), 1 cm diameter spheres of [^{18}O]H_2O, MeCN, DMSO, and glass were simulated. At the center of the sphere, simulated positrons were emitted isotropically according to the ^{18}F positron energy distribution. For S2 (Fig. 1b), two glass plates of 1 mm thickness sandwich a disk-shaped solvent droplet. Simulated positrons were isotropically emitted, uniformly within the solvent, according to the ^{18}F beta energy spectrum. Based on the EWOD chip geometry[28], the solvent radius and gap between the parallel glass plates of the EWOD chip were set to 3 mm and 0.15 mm, respectively. The solvent height was determined by the gap between the parallel glass plates of the EWOD chip. The extremely thin layers of indium tin oxide (140 nm), silicon nitride (2 μm and 100 nm layers on the bottom and top plates, respectively), and Teflon® AF (250 nm) that were present on the inner surfaces of the EWOD chips were ignored for simulation purposes. The contributions of Cerenkov photons produced from positrons traveling through the glass and solvent were considered separately. The solvent radius was then varied with the gap between glass plates being constant at 0.15 mm in order to determine the dependence of Cerenkov emission on solvent radius. The glass plate gap was also varied while keeping the solvent radius constant at 3 mm in order to determine the dependence of Cerenkov emission on solvent height.

2.2 Optical imaging system

An optical imaging chain has been devised to direct light into one of two cameras (Fig. 1c–1d). The setup was enclosed in a light tight enclosure (CSD20168, Hoffman, *Anoka, MN*) to eliminate the effect of ambient light on Cerenkov image quantification. A motorized rotation stage (PRM1Z8E, Thorlabs, *Newton, NJ*) was used to rotate a first surface mirror (Edmund Optics, *Barrington, NJ*) 45° from parallel with the chip towards either camera for Cerenkov imaging or video monitoring. The imaging system was placed in a fume hood, behind a lead L-block to shield the operator from radiation.

A DFK 21AU04 (Imaging Source, *Charlotte, NC*) camera utilizing a ICX098BQ (Sony, *Tokyo, Japan*) progressive scan CCD was coupled to a 5.0–50 mm variable focal length lens (MC Electronics, *Seoul, South Korea*). This camera was used to remotely monitor movement of fluids and other aspects of the radiochemical synthesis process on the EWOD device.

A QSI 540 (Quantum Scientific Imaging, *Poplarville, MS*) scientific cooled camera utilizing a KAI-04022 CCD (Kodak, *Rochester, NY*) was coupled to a fixed Nikkor 50 mm focal length lens (Nikon, *Tokyo, Japan*). This camera was used to assess the radioactive

distribution throughout the synthesis process via Cerenkov emission. A lead brick separated the CCD from the EWOD chip so as to reduce noise by decreasing the number of 511 keV annihilation photons that interacted directly with the CCD producing saturated or nearly saturated pixels. The Cerenkov camera was fixed to the light tight enclosure in order (i) to maintain reproducible distance between the camera and chip and (ii) to allow ventilation for camera cooling. The Cerenkov imaging camera's field of view was set to be approximately 5×5 cm^2, slightly greater than the dimensions of the EWOD chip. Exposure time was set to 30 seconds. Temperature of the CCD was set to −10°C to reduce dark current.

Cerenkov light emission has proven to be a promising tool in quantifying the amount of radioactivity within a microfluidic chip.[16,17] For a fixed geometry, we have previously shown a linear relationship between the Cerenkov signal and the radioactivity concentration.[16] Thus, to quantify the amount of radioactivity on the EWOD chip, a calibration of radioactivity in a droplet on the EWOD chip versus Cerenkov signal (expressed in the ADU pixel values of the CCD) was determined. Based on the initial work by Cho *et al*[16], three corrections were applied and are outlined here. (i) CCD dark current and bias level were corrected for by averaging 100 dark frames to create a master dark, which was subtracted from the image of interest. (ii) Lens vignetting and CCD pixel nonuniformity were accounted for by applying a master flat derived from 100 flat frame images. (iii) Lastly, to remove the effect of pixel saturation or near saturation by any 511 keV annihilation photons or cosmic rays that interacted directly with the Cerenkov camera, 3×3 median filtering was applied to the master dark and master flat corrected image.

Regions of interest (ROI) were drawn to encompass the radioactive distribution present on the image and a calibration factor was applied to determine the radioactivity within the ROI. For each experimental run, a sequence of images was taken to evaluate the radioactive distribution and the amount of radioactivity present on chip throughout the experimental procedure.

2.3 Simulation validation

The optical imaging system was used to examine Cerenkov photon yield for varying ratios of MeCN and DMSO in order to compare experiment with simulation. ~5 μL of [^{18}F]fluoride in [^{18}O]H_2O (radioactivity concentration: 0.1–0.2 mCi/μL) was pipetted into mixtures of MeCN and DMSO at varying ratios. Several ratios of mixtures of the three solvents were considered. In terms of the mass fraction of DMSO, m_{DMSO}, the ratios were 0.00, 0.34, 0.50, 0.63, and 0.87 (See Supplementary Fig. 1 for further information). From each mixture, a 5 μL droplet was pipetted and sandwiched between two Teflon coated glass plates with a gap height of 0.15 mm, mimicking the EWOD chip geometry. Each sandwiched droplet was placed at the center of the field of view of the Cerenkov camera. Acquisition time was set to 30 s. Immediately afterward, the sample was measured in the dose calibrator. Regions of interest were drawn around the imaged droplets. A calibration constant to convert measured Cerenkov signal to radioactivity was determined by dividing the ROI value (in units of ADU) by the acquisition time and by the measured amount of decay corrected radioactivity. The measurement set was performed twice. As a validation of the simulation, measurement points were plotted as a function of m_{DMSO} and overlaid with

the expected trend from simulation. For the simulated points, solvent mixtures were positioned according to S2. The simulated average numbers of Cerenkov photons were then normalized. For the i^{th} solvent mixture, the normalized simulated average Cerenkov photon yield, N_i, is given as:

$$N_i = S_i \frac{C_1}{S_1}$$

where S_i is the i^{th} simulated average Cerenkov photon yield, C_1 is the measured calibration factor for $m_{DMSO} = 0$, and S_1 is the simulated average Cerenkov photon yield for $m_{DMSO} = 0$. This was done in order to compare the simulated trend with the measured trend. The normalized trend was shifted by minimizing the square of differences between measurement and simulation.

2.4 EWOD chip fabrication and operation

EWOD chips and Teflon-coated glass substrates were fabricated as described by Keng *et al.*,[28] except that Teflon® AF 1600 (DuPont Fluoropolymer Solutions, *Wilmington, DE*) was used instead of Cytop® as the hydrophobic layer. Manipulation of liquids on the EWOD chip through the actuation of on-chip electrodes was carried out as described in Keng *et al.*[28]

2.5 Reagents

Mannose triflate was purchased from ABX GmbH (*Germany*) and used as received. Anhydrous acetonitrile (MeCN, 99.8%), anhydrous dimethyl sulfoxide (DMSO, 99.9%), potassium carbonate (99.9%), 4,7,13,16,21,24,-hexaoxa-1,10, diazobicyclo (8.8.8) hexacosane 98% (Kryptofix $K_{2.2.2}$), hexane, and ethyl acetate were purchased from Sigma-Aldrich and used as received without further purification. 1N HCl (certified, Fisher Chemicals) was purchased from Fisher Scientific and used as received. No-carrier-added [^{18}F]fluoride ion was obtained from the UCLA Crump Institute for Molecular Imaging Cyclotron and Radiochemistry Facility by irradiation of 97% ^{18}O-enriched water with an 11 MeV proton beam using an RDS-112 cyclotron (Siemens).

2.6 [^{18}F]FDG radiosynthesis and Cerenkov measurement sequence

2-[^{18}F]fluoro-2-deoxy-D-gluocse ([^{18}F]FDG) was synthesized based on a modification of the procedure reported by our group.[28] Briefly, a total of 16 μL (~0.5 mCi at start of synthesis) of [^{18}F]fluoride with $K_{2.2.2}$ (65 mM) and K_2CO_3 (17 mM) in 330:70 MeCN/H_2O was loaded onto the heater site in two portions as follows. Half the volume (8 μL) was loaded and a Cerenkov image was obtained. The radioactivity that was loaded on the chip was estimated by the amount of radioactivity removed from the source vial with a geometric correction factor applied to account for differences in dose calibrator response between the source vial and the EWOD chip (See Supplemental Fig. 2 for further information). Next, the 8 μL [^{18}F]KF/$K_{2.2.2}$ droplet was heated to 85 °C to evaporate some of the solvent. Removal of solvent vapor was assisted by nitrogen flow from one side of the chip. Afterwards, another 8 μL [^{18}F]KF/$K_{2.2.2}$ droplet was added and a second Cerenkov image was taken. The loaded radioactivity was again estimated from the source vial using a dose calibrator

measurement with a geometric correction factor applied. The solvent was then heated at 105 °C for 1 min and a dose calibrator measurement was taken of the chip. Subsequently, four 3 μL MeCN droplets were added to dissolve the [^{18}F]KF/$K_{2.2.2}$ residue. A third Cerenkov image was taken and associated with the previous dose calibrator measurement. The mixture was then heated at 105 °C for 1 min to evaporate the solvent. A dose calibrator measurement was taken of the dried EWOD chip. A 4 μL droplet of mannose triflate (104 mM) in DMSO was added to the dried [^{18}F]KF/$K_{2.2.2}$ residue. Electrowetting voltage was then applied in a periodic sequence from the inlet electrodes to the outer heater-electrode rings and then the inner rings. The 3 step sequence took about 3 seconds, and was repeated 5 times to induce mixing of the dried [^{18}F]KF/$K_{2.2.2}$ residue throughout the precursor solution. A fourth Cerenkov image was obtained at the end of the EWOD mixing process and associated with the previous dose calibrator measurement. Then, the mixture was gradually heated to 120 °C, and held at this temperature for 10 min to yield the intermediate product, 1,3,4,6-tetra-*O*-acetyl-beta-D-glucopyranose ([^{18}F]FTAG). A dose calibrator measurement was again taken. The crude [^{18}F]FTAG was hydrolyzed by adding five 3 μL droplets containing a 50:50 mixture of 1N HCl and MeCN, and a fifth Cerenkov image was taken and associated with the previous dose calibrator measurement. The mixture was then heated to 95 °C for 10 min. A sixth Cerenkov image was obtained followed by radioactivity measurement of the EWOD chip in a dose calibrator. Note that in some cases Cerenkov images were taken at slightly different time points because Cerenkov imaging measurements require some liquid to be present in the chip for consistency of the calibration constant, whereas dose calibrator measurements of the entire chip radioactivity were most practical on dry or nearly dry chips.

After the synthesis, the cover plate was removed and the crude [^{18}F]FDG product was extracted using 40 μL of H_2O and analyzed via radio-TLC.

The radiochemical yield was determined by dividing the amount of [^{18}F]FDG produced by the amount of [^{18}F]fluoride that was initially loaded onto the chip. The amounts, measured in units of radioactivity, were decay-corrected to a common time point. The amount of [^{18}F]FDG produced was estimated by multiplying the radioactivity of the recovered crude product from the chip (as determined by dose calibrator) by the fraction of radioactivity in the form of [^{18}F]FDG (as determined by radio-TLC). The amount of [^{18}F]fluoride loaded was estimated by measuring the source vial before and after adding the 16 μL of [^{18}F]fluoride onto the chip, also accounting for any radioactivity left in the pipette tips and gloves used in the pipetting procedure. This method has been verified to be within ~7% of the more cumbersome method of measuring the entire chip in the dose calibrator after the loading step. As described in the Results and Discussion, several small modifications to the synthesis protocol were made and evaluated to improve the synthesis yield.

2.7 Chromatography and analytical methods

Radioactivity was determined by placing samples in a calibrated ion chamber (CRC-15R, Capintec, Inc., *Ramsey, NJ*). To determine the radiofluorination efficiency, a sample aliquot was separated on a thin layer chromatography plate (JT Baker Flexible TLC sheet) using a 95:5 MeCN/H_2O solvent mixture as the mobile phase. To determine the hydrolysis efficiency via radio-TLC, the sample was separated using a 50:50 hexane/ethyl acetate

mixture as the mobile phase. Plates were scanned with a miniGITA Star radioactivity scanner (Raytest USA, Inc, *Wilmington, NC*) and chromatograms were analyzed with Gina Star TLC software (Raytest USA, Inc., *Wilmington, NC*).

Results and Discussion

3.1 Imaging system

We present an improved *in situ* radioactivity imaging system for microfluidics and use it to optimize the radiosynthesis of [^{18}F]FDG on a digital microfluidic chip. Compared to the previously reported Cerenkov imaging system,[16, 17] which used a single camera for both capturing the Cerenkov emission and for general observation of on-chip processes, the setup reported here used two cameras and a rotatable mirror to rapidly switch between the two imaging subsystems, each of which was optimized for its particular use (Fig. 1c–1d). A video camera was used to visualize droplet movement and heating on the EWOD chip under room light and a sensitive slow scan CCD camera (with a higher quantum efficiency than the camera used by Cho *et al.*[16]) was used to image the Cerenkov photons resulting from the interaction of positrons with the chemical reaction mixture and the chip itself. The use of a mirror provided the additional advantage of permitting the Cerenkov CCD camera to be shielded from direct gamma radiation emitted from the EWOD chip, which significantly reduced image noise.

3.2 Simulated average Cerenkov emission per ^{18}F decay

We first investigate the fundamental physical characteristics of Cerenkov photon yield to more reliably quantify the radioactivity at different stages of [^{18}F]FDG synthesis on the EWOD chip, and then we demonstrate the application of this tool to enable synthesis optimization. Radioactivity quantification using Cerenkov photon yield is complicated in this case because each solvent and material has a different index of refraction (n) and positron stopping power, and because different solvents (or solvent mixtures) are used during different steps of the synthesis. For example, [^{18}F]fluoride was produced in a solution of [^{18}O]H_2O (n = 1.33, ρ = 1.1 g/cm^3), the [^{18}F]fluoride loading process involved a mixture of MeCN (n = 1.34, ρ = 0.79 g/cm^3) and H_2O (n = 1.33, ρ = 1.0 g/cm^3), the [^{18}F]fluoride drying process involved MeCN, and the fluorination reaction of the [^{18}F]FDG synthesis was performed in a mixture of MeCN and DMSO (n = 1.48, ρ = 1.1 g/cm^3).

Fig. 2a compares the average Cerenkov emission per ^{18}F decay for selected materials according to the simulated geometries. S1 was performed in order to determine Cerenkov emission production from bulk amounts of materials of interest. The calculated average number of photons produced per ^{18}F decay is 1.7, 2.4, 3.1, and 5.1 in [^{18}O]H_2O, MeCN, glass, and DMSO, respectively. This suggests a possible doubling of photon yield as the solvent is changed from MeCN to DMSO and a tripling as the solvent is changed from [^{18}O]H_2O to DMSO. This dependence of Cerenkov photon yield on material properties for bulk quantities complicates the calculation of a calibration factor throughout the [^{18}F]FDG synthesis to translate Cerenkov photon signal to radioactivity.

However, the nearly planar geometry of EWOD suggests that most of the ^{18}F beta energy will be deposited in the glass rather than the solvent mixture. To validate our hypothesis, S2 was developed to examine Cerenkov emission produced within the EWOD geometry. The calculated average number of photons produced per decay is 2.7, 3.0, and 3.8 for droplets of $[^{18}O]H_2O$, MeCN and DMSO, respectively. This simulation suggests a significant reduction in the range of average Cerenkov emission per ^{18}F decay for the solvents examined. Furthermore, in Fig. 2a, the glass and solvent contributions to Cerenkov production are separated and show that approximately two-thirds of the [^{18}F]fluoride positron energy available for Cerenkov photon production is deposited in the glass. This is consistent with Rensch *et al.*[32] who showed in geometries with dimensions comparable to microfluidic devices, radiolysis can be significantly reduced because much of the positron energy is deposited in the walls rather than the liquid. Despite the mitigating effect of the EWOD geometry, there is still a small difference in the simulated light output depending on the type of solvent present in the droplet.

Since the volume of the droplet is different at different points during the synthesis process, the dependence of photon yield on solvent geometry was also considered using S2. Given a fixed droplet height of 0.15 mm, the average Cerenkov emission per ^{18}F decay remains constant above a droplet radius of 1 mm (Fig. 2b). This corresponds to a volume of ~0.5 μL. Since for most practical situations the droplet volume is larger than this at the time points of interest, we can therefore assume the droplet radius has negligible effect on the Cerenkov signal.

We also examined the effect of changing the droplet height using S2 as there are small manufacturing variations in the gap height from one chip to another, and it is desirable to have a single calibration that can be used for all chips. Given a fixed solvent radius of 3 mm, Cerenkov emission was compared for gap heights in the range 0.100 to 0.200 mm (Fig. 2c). For MeCN, there is negligible difference in the simulated Cerenkov output over the entire range of geometries. For DMSO and [^{18}O]H2O, the maximum deviation is less than 5% from the nominal value at 0.150 mm gap height. Since 0.050 mm is much greater than the expected chip to chip variation, we can therefore assume these variations to have neglible effect on the Cerenkov signal and thus a single calibration can be used for all chips.

3.3 Dependence of calibration on index of refraction

Experimental validation of the simulated results was conducted to evaluate the extent of Cerenkov photon production in the glass as opposed to the solvent. The ratio of Cerenkov measured signal rate, in units of ADU normalized by acquisition time, to decay corrected radioactivity, serves as the calibration factor to convert the measured signal to radioactivity. In Fig. 2d, measurements of the calibration value for different solvent ratios are plotted as a function of the mass fraction of DMSO, m_{DMSO}. It can be seen that there is negligible measured difference in observed light output, and therefore calibration constant, despite the wide variation in mixture composition. The constancy of the measured calibration value as a function of varying solvent ratios indicates that the majority of ^{18}F positrons that originate in the solvent do in fact deposit most of their energy in the glass.

From the simulation in Fig. 2a, a modest difference in light output is expected depending on solvent. The expected trend from simulation of solvent mixtures is overlayed on Fig. 2d. It can be presumed that the deposition of positron energy in glass is modestly underestimated in the simulation.

3.4 Cerenkov image quantitation during [^{18}F]FDG synthesis

Fig. 3a shows decay corrected radioactivity calculated from Cerenkov images of the EWOD chip during the synthesis of [^{18}F]FDG alongside values determined from the dose calibrator. The calibration constant was set by the first [^{18}F]fluoride loading step. Results of the measurements correspond very well except for the last two measurements. The good agreement at a variety of steps, where different solvents are present in the chip, suggests that indeed the Cerenkov measurements are in practice independent of solvent, and a single calibration constant suffices throughout the synthesis. Cerenkov imaging measurements though indicate significant losses of radioactivity after fluorination (Fig. 3a, step 5) and hydrolysis (Fig. 3a, step 6) in contrast to the dose calibrator measurements that indicate only very small losses. We suspect this discrepancy is due to the discoloration of the droplet at this stage of the synthesis (Fig. 3b–3f). The reaction droplet turns from clear to brown during these two processes. This discoloration considerably reduces the amount of Cerenkov light detected by the CCD due to light absorption within the droplet. Determining the influence of coloration on Cerenkov output will involve many factors including the light absorption spectrum of the solute/solvent and the droplet geometry, and can form the basis for an interesting study in the future. For clear liquids, our studies have shown that the amount of radioactivity can be accurately quantified in regions of interest in the microfluidic chip using a single calibration constant.

In situ Cerenkov imaging avoids the cumbersome process of removing and reinstalling the chip that is needed for dose calibrator measurements, thus reducing the operator's radiation exposure and minimizing the opportunities for errors. In addition, the dose calibrator provides only a single radioactivity measurement for the whole chip, but Cerenkov imaging can provide spatially resolved measurements.

3.5 Optimizing radiochemistry on-chip via *in situ* Cerenkov imaging

The limiting reagent in a radiochemical synthesis is the radioisotope. For example, only a few picomole of [^{18}F]fluoride ions are present in a synthesis at the 10 mCi scale (approximate amount injected for PET scan of a single human patient). Therefore, it is critical to develop an optimal methodology for on-chip manipulation of the radioactive solution throughout the synthesis to avoid losses which reduce the overall radiochemical yield. In the remainder of this section, we demonstrate the application of Cerenkov imaging to optimize the microfluidic synthesis of [^{18}F]FDG, obtaining an increase in the crude radiochemical yield from 50±3% (n=3) to 72±13% (n=5). By comparing Cerenkov images captured at different time-points of the synthesis, it was possible to make several significant improvements in the process as described below.

3.5.1 Radioactivity loading—Cerenkov images were obtained after each [^{18}F]fluoride solution loading step, and we found in both cases that all radioactivity was confined within

the droplet where liquid was present. When comparing the images after the first and second loading steps, doubling of the amount of on-chip radioactivity was confirmed (Fig. 3a, step 1 and 2). This further suggests there is negligible loss during the evaporation process after the first loading step.

3.5.2 Evaporation, solvent exchange and precursor loading—After evaporation of the solvent in the loaded [^{18}F]fluoride solution, MeCN was added and a Cerenkov image was obtained (Fig. 3a, step 3). The image showed negligible change in the amount of radioactivity. After azeotropic distillation (addition and evaporation of MeCN) was performed, the precursor solution was loaded and another Cerenkov image was taken (Fig. 3a, step 4). Again, negligible change in radioactivity was observed, suggesting there are negligible losses during evaporation.

3.5.3 Mixing—Comparison of video and Cerenkov images taken after loading mannose triflate in DMSO enabled optimization of the amount of MeCN droplets needed to be added to completely re-dissolve the dried [^{18}F]KF/$K_{2.2.2}$ complex at the reaction site on the chip. Non-dissolved residue would not be able to participate in the subsequent fluorination reaction and would thus reduce the overall yield. The Cerenkov image of the dried droplet at this step provides only a qualitative picture of the radioactivity distribution before the initial MeCN is added because some areas of radioactive residue are not covered with solvent. The lack of solvent creates a different environment for beta particles and the Cerenkov photons they produce, and therefore, it is likely that this image requires a different calibration to accurately relate the detected light output to radioactivity. Nonetheless, this qualitative observation of the radioactive residue distribution after the drying steps enables determination of the required volume of solvent to fully cover the radioactive footprint. Upon determining the optimal volume of MeCN needed, the same protocol was then applied to subsequent [^{18}F]FDG syntheses.

In our previous report, we mixed the droplet by heating at 60°C for 3 min.[28] It is hypothesized that the heating leads to internal convection and more rapidly mixes the droplet than diffusion alone (Fig. 4a–4b). Using Cerenkov imaging to monitor the uniformity of re-dissolved [^{18}F]KF/$K_{2.2.2}$ residue, we show here an even faster mixing process. By applying EWOD actuation potential to the heater electrodes it was possible to move the mixture back and forth across the solid residue. After only 30 sec of EWOD-actuated mixing, the distribution of radioactivity had good homogeneity (Fig. 4c–4d).

3.5.4 Fluorination and hydrolysis reactions—Due to the open structure of the EWOD chip, the majority of the solvent evaporates during the 10 min fluorination reaction (at 120 °C), leaving only a small solvent droplet containing [^{18}F]FTAG on the heater electrode at the end of this process. In our initial investigations, we observed a significantly reduced amount of radioactivity in the region of the droplet after the reaction as compared to before and assumed it was completely lost from the chip as a gas or aerosol. Upon careful analysis of post-fluorination Cerenkov images, we discovered a large region with faint Cerenkov signal outside the heater electrodes. Integrated over the whole region, we found a significant amount of radioactivity. This region was on the side of the heater opposite the source of the nitrogen stream. Comparison with video images revealed that the radioactivity

coincided with the location of what we assumed was vapor condensation. (The temperature of the chip away from the heater electrodes is cooler and can cause vapor to condense during times when the heater electrodes are activated.) We found that the radioactivity extracted from the condensates using a mixture of methanol and water consisted of 5–14% of the total radioactivity measured on-chip (Fig. 5a). Radio-TLC analysis of the condensates showed that the majority of the radioactivity was in the form of unreacted [^{18}F]fluoride ion, while a smaller percentage (~32%) was the fluorinated product, [^{18}F]FTAG (Fig. 5a). Based on these results, we hypothesized that if we could pause the reaction, move the condensates back to the heater, and continue the reaction, that we might be able to improve the yield by up to 4–10%. We therefore designed a new chip layout to enable much of the condensates area to be “rinsed” and the contents transported back to the heater region. In comparison to our previous chip design, the new chip design consisted of two additional inlet pathways labeled **Inlet 4** and **Inlet 5** in Fig. 5a.

On the new chip, a rinsing step was added after 5 min of fluorination to wash and merge the radioactive condensates to the parent droplet (Fig. 5b–5c). The merged droplet was moved to the center of the EWOD heater and the fluorination reaction was continued at 120 °C for another 5 min. As a result of this change, the overall crude radiochemical yield of [^{18}F]FDG improved from 50±3 (n=3) to 72±13 (n=5) suggesting that indeed much of the collected unreacted [^{18}F]fluoride indeed underwent the fluorination reaction after remerging with the main droplet.

The ability to conveniently capture Cerenkov images at many time points throughout a multi-step synthesis process provided many opportunities to non-destructively measure the performance of individual steps. The result of process changes could be rapidly evaluated, resulting in significant acceleration of optimization.

4. Conclusion

We investigated the fundamental physical characteristics of Cerenkov photon yield at different stages of the [^{18}F]FDG synthesis on the EWOD chip. Our EWOD simulation suggests that the nearly planar geometry of the chip causes the majority of ^{18}F positron energy available to produce Cerenkov emission to be deposited in the glass rather than the droplet. As a result, it may be possible for one calibration factor to convert Cerenkov signal to radioactivity independent of solvent composition. We validated our simulations with controlled measurements examining varying ratios of [^{18}O]H_2O, DMSO, and MeCN, and found a consistent calibration independent of solvent composition. We furthermore observed good agreement between quantitative measurements of radioactivity via Cerenkov imaging and via the use of a dose calibrator. One limitation is that the calibration factor underestimates the radioactivity if the droplet becomes discolored during the synthesis of a radiolabeled probe. Further work will involve developing a procedure to correct for this discoloration. We also plan to elaborate on our simulation, and, in addition to generation, we will investigate Cerenkov photon transport and detection in order to explore Cerenkov light losses due to issues such as total internal reflection and absorption within the chip.

In addition to the quantitative accuracy of Cerenkov imaging, this imaging strategy provides indispensable *in situ* qualitative information to be gleaned about the synthesis. We were able to use this imaging technique to optimize the mixing protocol as well as identify and correct for the loss of ^{18}F available for reaction due to its migration outside the heater.

Although this work focuses on [^{18}F]FDG synthesis, Cerenkov imaging can be extended as a general tool for the optimization of syntheses or assays on microfluidic chips involving suitable electron- as well as positron-emitting radiolabeled compounds of interest. As Cerenkov emission is dependent on the beta particle energy distribution of a specific radioisotope as well as chip geometry, each radioisotope will require its own calibration factor to convert observed Cerenkov signal to radioactivity.[25] Consequently, Cerenkov imaging has the potential to be used as a means to image pure electron emitters such as ^{32}P, ^{90}Y, and ^{131}I used, for example, as part of labeling proteins, DNA and RNA, or as part of synthesizing radiotherapies in order to optimize the radiolabeling procedure on a microfluidic chip. [21, 33]

Supplementary Material

Refer to Web version on PubMed Central for supplementary material.

Acknowledgments

This work was supported in part by the National Institute of Health (R25CA098010), the Department of Energy (DE-SC0005056, DE-SC0001249), the UCLA Department of Molecular and Medical Pharmacology, and the UCLA Foundation from a donation made by Ralph & Marjorie Crump for the UCLA Crump Institute for Molecular Imaging. We thank Dr. David Stout at the Crump Radiochemistry Cyclotron facility and Dr. Saman Sadeghi at the UCLA Biomedical Cyclotron facility for providing [^{18}F]fluoride ion for these studies

Notes and references

1. Schumacher, TN.; Tsomides, TJ. Current Protocols in Protein Science. John Wiley & Sons, Inc.; 2001. p. 3.3.1-3.3.19.
2. Strachan, T.; Read, A. Chapter 5, Nucleic acid hybridization assays; Chapter 6, PCR, DNA sequencing and in vitro mutagenesis. New York: Wiley-Liss; 1999.
3. Imam SK. Cancer Biother Radiopharm. 2005; 20:163–172. [PubMed: 15869450]
4. Sharkey RM, Goldenberg DM. Immunotherapy. 2011; 3:349–370. [PubMed: 21395378]
5. Eckelman WC, Paik CH, Reba RC. Cancer Research. 1980; 40:3036–3042. [PubMed: 7397697]
6. Audrain H. Angewandte Chemie International Edition. 2007; 46:1772–1775.
7. Lu SY, Pike VW. Ernst Schering Res Found Workshop. 2007:271–287. [PubMed: 17172159]
8. Elizarov AM. Lab on a Chip. 2009; 9:1326–1333. [PubMed: 19417895]
9. Miller PW, deMello AJ, Gee AD. Current Radiopharmaceuticals. 2010; 3:254–262.
10. Keng PY, Esterby M, van Dam RM. Emerging Technologies for Decentralized Production of PET Tracers. 2012
11. Lavén M, Velikyan I, Djodjic M, Ljung J, Berglund O, Markides K, Långström B, Wallenborg S. Lab on a Chip. 2005; 5:756–763. [PubMed: 15970969]
12. Fang C, Wang Y, Vu NT, Lin W-Y, Hsieh Y-T, Rubbi L, Phelps ME, Müschen M, Kim Y-M, Chatziioannou AF, Tseng H-R, Graeber TG. Cancer Research. 2010; 70:8299–8308. [PubMed: 20837665]
13. Vu NT, Yu ZTF, Comin-Anduix B, Søndergaard JN, Silverman RW, Chang CYN, Ribas A, Tseng H-R, Chatziioannou AF. Journal of Nuclear Medicine. 2011; 52:815–821. [PubMed: 21536929]

14. Dooraghi AA, Vu NT, Silverman RW, Farrell R, Shah KS, Wang J, Heath JR, Chatziioannou AF. Physics in Medicine and Biology. 2013; 58:3739. [PubMed: 23656911]
15. Sadeghi S, Liang V, Cheung S, Woo S, Wu C, Ly J, Deng Y, Eddings M, van Dam RM. Applied Radiation and Isotopes. 2013; 75:85–94. [PubMed: 23474380]
16. Cho JS, Taschereau R, Olma S, Liu K, Chen Y-C, Shen CKF, van Dam RM, Chatziioannou AF. Physics in Medicine and Biology. 2009; 54:6757. [PubMed: 19847018]
17. Tseng W-Y, Cho JS, Ma X, Chen Y-C, Kunihiro A, Mahal K, Chatziioannou AF, van Dam RM. unpublished work.
18. Lee C-C, Sui G, Elizarov A, Shu CJ, Shin Y-S, Dooley AN, Huang J, Daridon A, Wyatt P, Stout D, Kolb HC, Witte ON, Satyamurthy N, Heath JR, Phelps ME, Quake SR, Tseng H-R. Science. 2005; 310:1793–1796. [PubMed: 16357255]
19. Elizarov AM, van Dam RM, Shin YS, Kolb HC, Padgett HC, Stout D, Shu J, Huang J, Daridon A, Heath JR. Journal of Nuclear Medicine. 2010; 51:282–287. [PubMed: 20124050]
20. Robertson R, Germanos MS, Li C, Mitchell GS, Cherry SR, Silva MD. Physics in Medicine and Biology. 2009; 54:N355. [PubMed: 19636082]
21. Xu Y, Liu H, Cheng Z. Journal of Nuclear Medicine. 2011; 52:2009–2018. [PubMed: 22080446]
22. Boschi F, Calderan L, D'Ambrosio D, Marengo M, Fenzi A, Calandrino R, Sbarbati A, Spinelli AE. European Journal of Nuclear Medicine and Molecular Imaging. 2011; 38:120–127. [PubMed: 20882278]
23. Jeong SY, Hwang M-H, Kim JE, Kang S, Park JC, Yoo J, Ha J-H, Lee S-W, Ahn B-C, Lee J. Endocrine Journal. 2011; 58:575–583. [PubMed: 21551958]
24. Li C, Mitchell GS, Cherry SR. Opt. Lett. 2010; 35:1109–1111. [PubMed: 20364233]
25. Ruggiero A, Holland JP, Lewis JS, Grimm J. Journal of Nuclear Medicine. 2010; 51:1123–1130. [PubMed: 20554722]
26. Beattie BJ, Thorek DLJ, Schmidtlein CR, Pentlow KS, Humm JL, Hielscher AH. PLoS ONE. 2012; 7:e31402. [PubMed: 22363636]
27. Mitchell GS, Gill RK, Boucher DL, Li C, Cherry SR. Philosophical Transactions of the Royal Society A: Mathematical, Physical and Engineering Sciences. 2011; 369:4605–4619.
28. Keng PY, Chen S, Ding H, Sadeghi S, Shah GJ, Dooraghi A, Phelps ME, Satyamurthy N, Chatziioannou AF, Kim C-J, van Dam RM. Proceedings of the National Academy of Sciences. 2011
29. Agostinelli S, Allison J, Amako K, Apostolakis J, Araujo H, Arce P, Asai M, Axen D, Banerjee S, Barrand G, Behner F, Bellagamba L, Boudreau J, Broglia L, Brunengo A, Burkhardt H, Chauvie S, Chuma J, Chytracek R, Cooperman G, Cosmo G, Degtyarenko P, Dell'Acqua A, Depaola G, Dietrich D, Enami R, Feliciello A, Ferguson C, Fesefeldt H, Folger G, Foppiano F, Forti A, Garelli S, Giani S, Giannitrapani R, Gibin D, Gómez Cadenas JJ, González I, Gracia Abril G, Greeniaus G, Greiner W, Grichine V, Grossheim A, Guatelli S, Gumplinger P, Hamatsu R, Hashimoto K, Hasui H, Heikkinen A, Howard A, Ivanchenko V, Johnson A, Jones FW, Kallenbach J, Kanaya N, Kawabata M, Kawabata Y, Kawaguti M, Kelner S, Kent P, Kimura A, Kodama T, Kokoulin R, Kossov M, Kurashige H, Lamanna E, Lampén T, Lara V, Lefebure V, Lei F, Liendl M, Lockman W, Longo F, Magni S, Maire M, Medernach E, Minamimoto K, Mora de Freitas P, Morita Y, Murakami K, Nagamatu M, Nartallo R, Nieminen P, Nishimura T, Ohtsubo K, Okamura M, O'Neale S, Oohata Y, Paech K, Perl J, Pfeiffer A, Pia MG, Ranjard F, Rybin A, Sadilov S, Di Salvo E, Santin G, Sasaki T, Savvas N, Sawada Y, Scherer S, Sei S, Sirotenko V, Smith D, Starkov N, Stoecker H, Sulkimo J, Takahata M, Tanaka S, Tcherniaev E, Safai Tehrani E, Tropeano M, Truscott P, Uno H, Urban L, Urban P, Verderi M, Walkden A, Wander W, Weber H, Wellisch JP, Wenaus T, Williams DC, Wright D, Yamada T, Yoshida H, Zschiesche D. Nuclear Instruments and Methods in Physics Research Section A: Accelerators, Spectrometers, Detectors and Associated Equipment. 2003; 506:250–303.
30. Allison J, Amako K, Apostolakis J, Araujo H, Dubois PA, Asai M, Barrand G, Capra R, Chauvie S, Chytracek R, Cirrone GAP, Cooperman G, Cosmo G, Cuttone G, Daquino GG, Donszelmann M, Dressel M, Folger G, Foppiano F, Generowicz J, Grichine V, Guatelli S, Gumplinger P, Heikkinen A, Hrivnacova I, Howard A, Incerti S, Ivanchenko V, Johnson T, Jones F, Koi T, Kokoulin R, Kossov M, Kurashige H, Lara V, Larsson S, Lei F, Link O, Longo F, Maire M,

Mantero A, Mascialino B, McLaren I, Lorenzo PM, Minamimoto K, Murakami K, Nieminen P, Pandola L, Parlati S, Peralta L, Perl J, Pfeiffer A, Pia MG, Ribon A, Rodrigues P, Russo G, Sadilov S, Santin G, Sasaki T, Smith D, Starkov N, Tanaka S, Tcherniaev E, Tome B, Trindade A, Truscott P, Urban L, Verderi M, Walkden A, Wellisch JP, Williams DC, Wright D, Yoshida H. Nuclear Science, IEEE Transactions on. 2006; 53:270–278.

31. Kozma IZ, Krok P, Riedle E. Opt. Soc. Am. B. 2005; 22:1479–1485.
32. Rensch C, Waengler B, Yaroshenko A, Samper V, Baller M, Heumesser N, Ulin J, Riese S, Reischl G. Appl Radiat Isot. 2012; 70:1691–1697. [PubMed: 22750198]
33. Spinelli AE, Ferdeghini M, Cavedon C, Zivelonghi E, Calandrino R, Fenzi A, Sbarbati A, Boschi F. Journal of Biomedical Optics. 2013; 18:020502–020502.

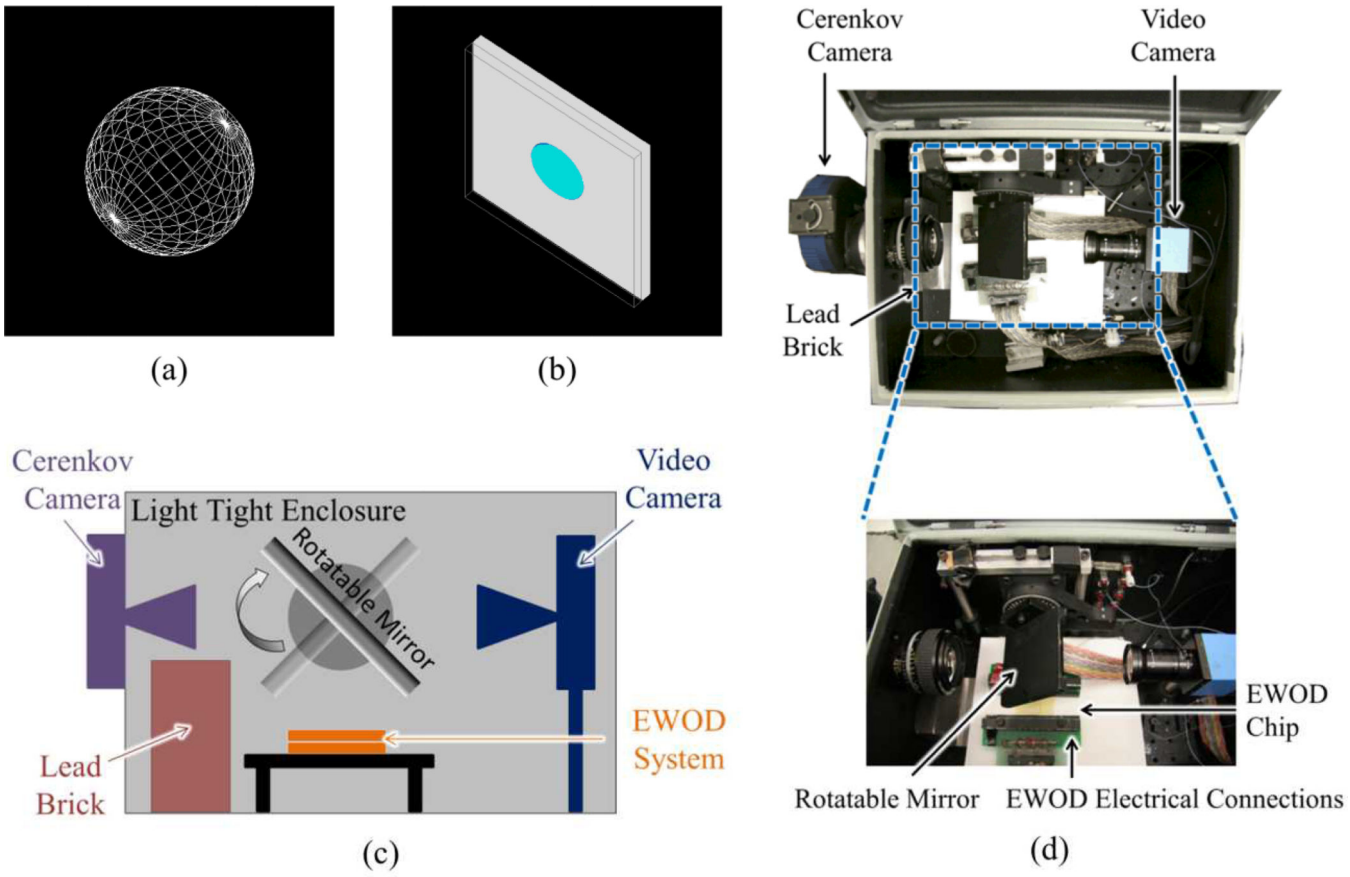

Fig. 1.

(a) Simulation 1 (S1) geometry consisting of a 1 cm in diameter sphere of material of interest. Simulated positrons are emitted from the center according to the ^{18}F beta energy spectrum. (b) Simulation 2 (S2) geometry consisting of two glass plates of 1 mm thickness that sandwich a cylindrical droplet of solvent. Simulated positrons are isotropically emitted from a uniform distribution within the solvent according to the ^{18}F beta energy spectrum. Solvent radius is 3 mm and solvent height, which is set by the gap between the parallel glass plates, is 0.15 mm. (c) Schematic of the imaging setup. (d) *Top*: Photograph looking down at the EWOD radiosynthesis chip set up inside the light-tight box of the Cerenkov imaging system. *Bottom*: The EWOD chip is located underneath a pivoting mirror that directs light to either the Cerenkov camera (left) or the video camera (right).

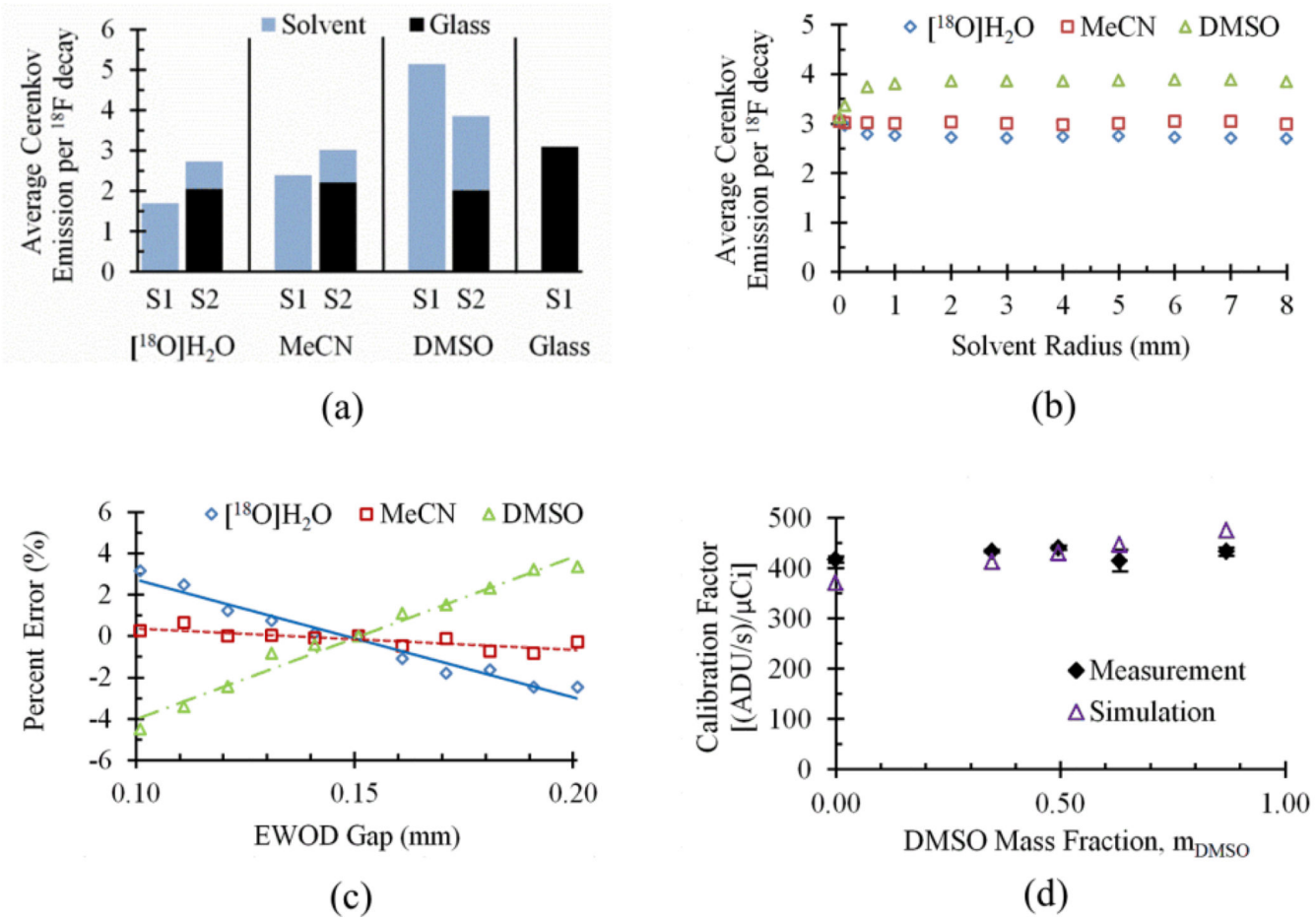

Fig. 2.

(a) Comparison of average Cerenkov emission per ^{18}F decay for selected materials according to S1 and S2. For S2, the contribution of Cerenkov photons from the glass and from the solvent are separated. (b) Graph of dependence in S2 of average Cerenkov emission per ^{18}F decay on solvent radius. (c) Graph of dependence in S2 of average Cerenkov emission per ^{18}F decay on gap between parallel glass plates. (d) Graph of calibration factor (ratio of Cerenkov emission rate to decay corrected activity) for different mass fractions of DMSO in a solvent mixture of DMSO, MeCN and [^{18}O]H$_2$O.

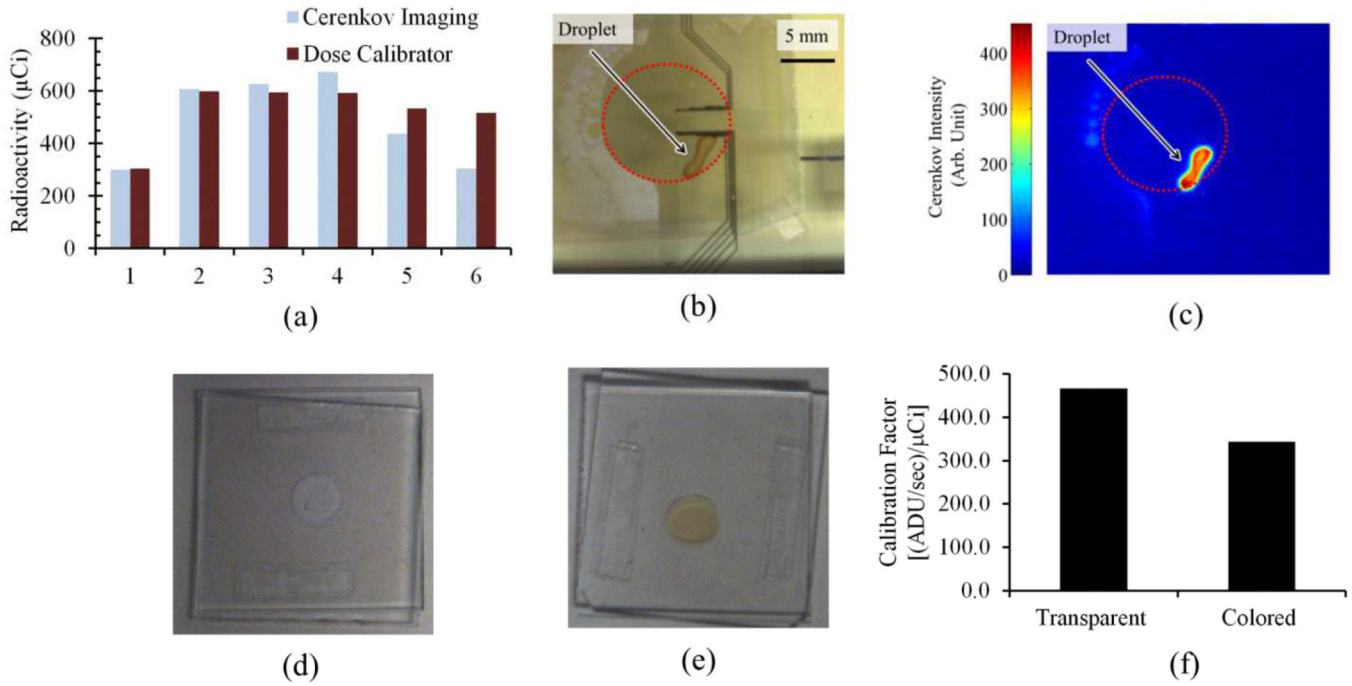

Fig. 3.

(a) Representative study of radioactivity calculated from Cerenkov images alongside values determined from dose calibrator at six different stages of [^{18}F]FDG synthesis on chip. 1: After loading first half of [^{18}F]fluoride solution; 2: After loading second half; 3:After evaporating solvent (dose calibrator) then adding MeCN (Cerenkov); 4:After MeCN evaporation (dose calibrator) then adding precursor solution (Cerenkov); 5: After fluorination reaction (dose calibrator) then adding HCl/MeCN solution (Cerenkov); 6: After hydrolysis reaction. Note that in some cases Cerenkov images are taken at slightly different time points because Cerenkov measurements require some liquid to be present in the chip for consistency with calibration constant whereas dose calibrator measurements are most practical on dry or nearly dry chips. For time points 1 and 2, dose calibrator measurements are estimated from the amount of radioactivity removed from the source vial with a small geometric correction factor applied. (b) Representative video image illustrating discoloration of the droplet at the end of the hydrolysis reaction. (c) The corresponding Cerenkov image. (d–e) Video images of droplets (~5μL) of [^{18}F]fluoride diluted in water (d) without and (e) with the addition of caramelized glucose to study the effect of liquid discoloration. (f) Resulting measured calibration factors. Discoloration results in a reduction in detected Cerenkov photons and consequently would lead to an underestimation of radioactivity measurements when a calibration from a transparent source is used.

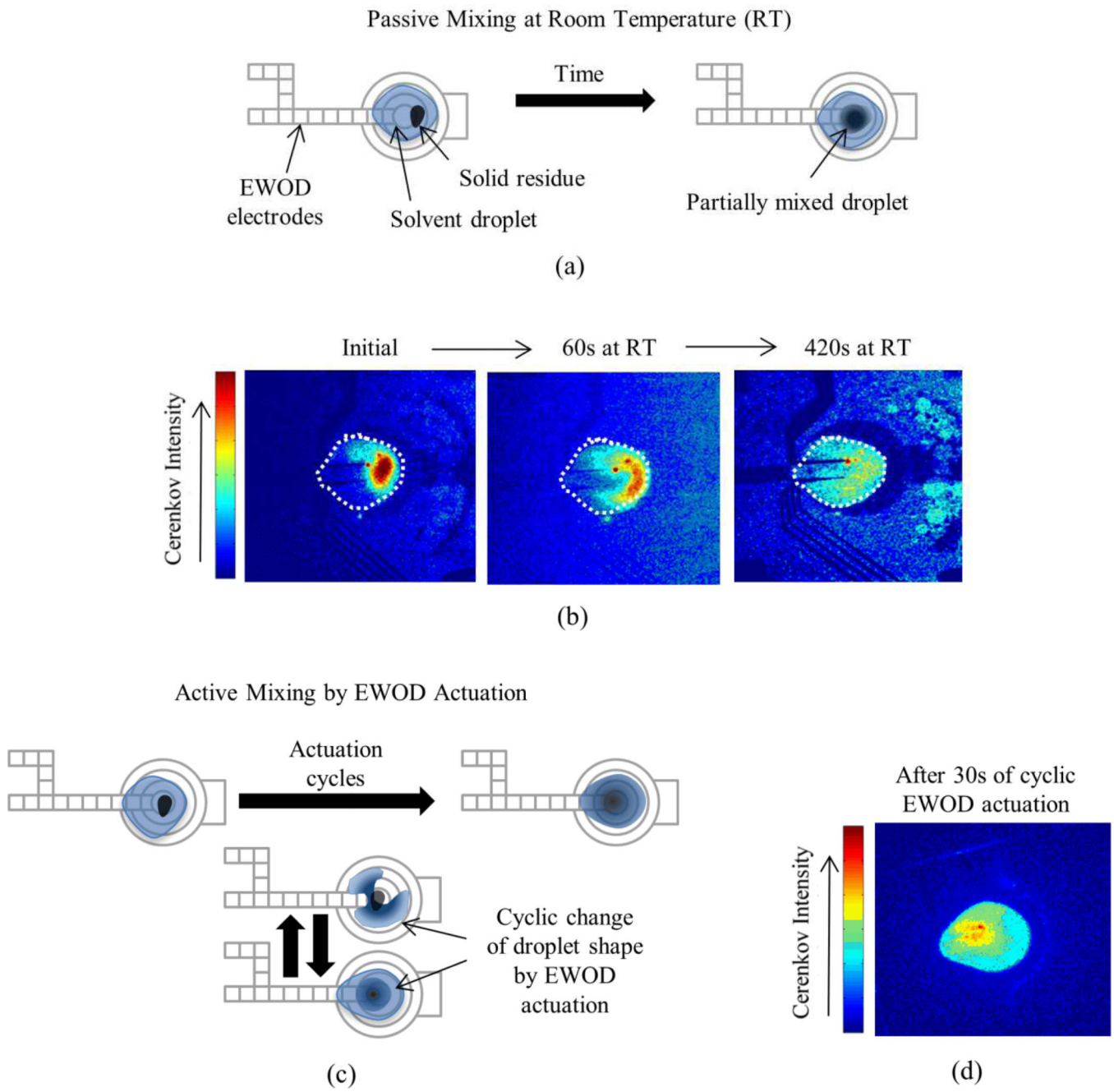

Fig. 4.

Comparison of different mixing techniques on the EWOD chip. (a) Schematic of passive mixing at room temperature. (b) Cerenkov images during passive mixing process. White dots represent perimeter of droplet. (c) Schematic of active mixing process by cyclic actuation of EWOD electrodes. (d) Cerenkov image after EWOD actuated mixing for 30s.

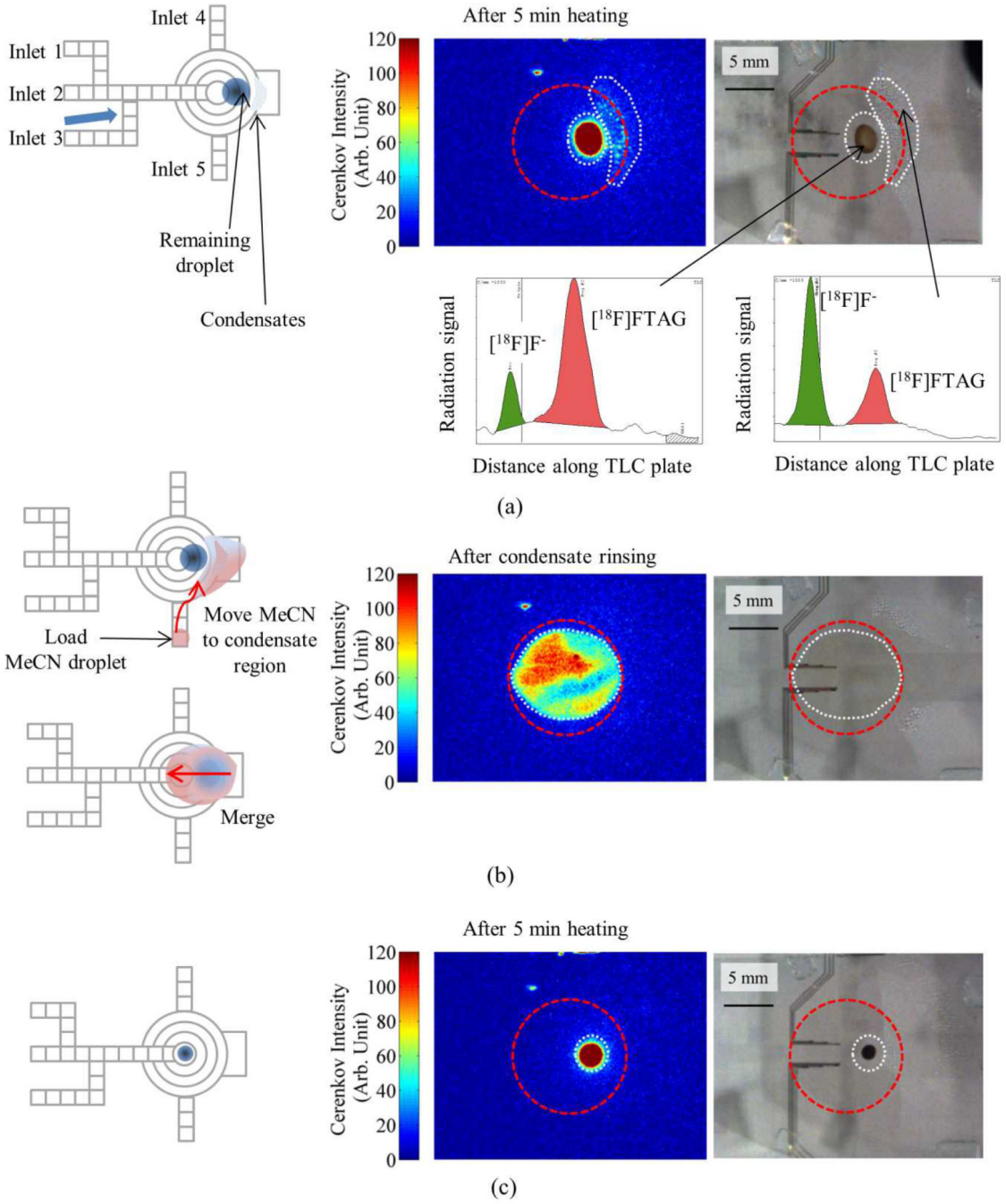

Fig. 5.

Improved fluorination process. (a) Using a modified chip with two extra reagent inlets (4 and 5) the overall yield could be improved. The blue arrow represents the direction of nitrogen flow during the reaction step. Images are of the chip after 5 min of the fluorination reaction and cooling of the chip to room temperature, showing the remaining reaction droplet and a region of condensation. The heater region is marked wtih a red-dashed circle and the droplet is marked with a white dashed line for visual clarification of Cerenkov and video images. The radio-TLC chromatogram shows the composition of the radioactive

species in the condensates from a typical experiment. (b) Several MeCN droplets (orange colored circle) were loaded through inlet 5 and transported via EWOD to the condensate region. The merged droplet was then transported to the center of the heater to merge with the main reaction droplet. Images show the result of this merging process. (c) The fluorination reaction was continued for 5 min, yielding a single, small reaction droplet and no apparent radioactivity outside the droplet.

Table 1

Physical properties of materials considered in study relevant to Cerenkov emission. Index of refraction is quoted at the Fraunhofer “D” line (wavelength: 589.29 nm)

Material	Index of refraction, n_D	Density, ρ [g/cm^3]
[^{18}O]H_2O	1.33	1.10
DMSO	1.48	1.10
MeCN	1.34	0.79
Glass	1.52	2.53